Acta Geodaetica et Geophysica (2025) 60:465–480
https://doi.org/10.1007/s40328-025-00480-3

ORIGINAL STUDY

Gravitational field modeling of irregularly shaped bodies by solving the coupled interior-exterior boundary value problem

Marek Macák[1] · **Zuzana Minarechová**[1] · **Karol Mikula**[1]

Received: 15 August 2025 / Accepted: 24 November 2025 / Published online: 8 December 2025

Abstract
In this paper, we propose and apply a novel numerical approach for modeling the gravitational field by solving the coupled interior-exterior boundary value problem (BVP) using the finite element method (FEM). To this end, we construct a finite computational domain encompassing the selected celestial object and a bounded portion of its exterior, within which the BVP is formulated. This problem consists of the Poisson equation for the gravitational potential, along with a Dirichlet boundary condition (BC) prescribed on the boundary. In this case, since the boundary is placed far from the object so that the Dirichlet BC is nearly zero, the only key input for the computation is the 3D model of the celestial body and its density. The solution is derived using the FEM, which is particularly effective for handling highly irregular or complex surface geometries. The numerical experiments include a test case involving a homogeneous sphere to demonstrate the second-order accuracy of the proposed approach as well as simulations of the gravitational fields of two selected asteroids, namely 25143 Itokawa and 433 Eros, and the comet 67P/Churyumov-Gerasimenko. These simulations yield detailed three-dimensional distributions of both gravitational potential and gravitational acceleration within the entire computational domain.

Keywords Gravitational field modelling · Interior-exterior boundary-value problem · The finite element method · Irregularly shaped bodies

✉ Zuzana Minarechová
zuzana.minarechova@stuba.sk

Marek Macák
marek.macak@stuba.sk

Karol Mikula
karol.mikula@stuba.sk

[1] Faculty of Civil Engineering, Slovak University of Technology, Radlinského 11, 810 05 Bratislava, Slovakia

1 Introduction

Advancements in science and technology have significantly expanded the possibilities for exploring celestial bodies. Modern instruments, spacecraft, and observation techniques now allow scientists to study planets, moons, asteroids, and other objects in space, helping us better understand the origins and nature of the universe. Several space missions, e.g. Hayabusa (Yoshikawa et al. 2021), Hayabusa2 (Tsuda et al. 2013), Rosetta (Taylor et al. 2017), OSIRIS-REx (March 2021), Lucy (Olkin 2021), and Psyche (Zuber et al. 2022), have been launched to explore comets and asteroids, and their number is expected to increase in the coming years. Thanks to these missions, we are able to obtain a wealth of valuable information about our solar system and its formation. Since most asteroids and comets have highly irregular shapes and unknown mass distributions, having detailed knowledge of their gravitational potential is crucial for spacecraft approaching them. Moreover, such studies can also advance our research of the Earth's gravity field, where each year we gain increasingly detailed information about both the terrain itself and the gravitational field, including its temporal variations.

The determination of the gravitational and gravity fields is usually formulated in terms of geodetic boundary value problems (BVPs), the foundations of which were first laid in publications such as Legendre (1782); Laplace (1785, 1799). Nowadays, the most commonly employed methods for modeling the Earth's gravity field are those based on spherical and spheroidal harmonic functions (e.g., Moritz (1980); Sanso and Sideris (2013)). For irregular celestial bodies, however, the use of spherical harmonics may be problematic due to poor convergence near the surface, where the discrepancy between the actual shape and the assumed spherical reference leads to significant modeling errors. Alternative approaches and applications tailored to celestial bodies can be found in, e.g., Sebera et al. (2016); Bucha et al. (2019); Šprlák et al. (2020); Bucha and Sansó (2021) and the references therein.

On the other hand, for celestial bodies, the most widely used approaches are the mascon (mass concentration) technique and the polyhedral method. The main idea behind the mascon technique is to approximate the actual body by a discrete system of point masses or small volumetric elements, each assigned a specific mass concentration. These mascons are strategically distributed to accurately represent the true internal mass distribution of the body. For more details, see e.g. Geissler et al. (1996); Park et al. (2010); Colagross et al. (2015); Chanut et al. (2015). The principle of the polyhedral method consists of modeling the body as a convex or non-convex polyhedron composed of triangular or quadrilateral faces. Based on this model, the gravitational potential and gravitational acceleration at any point in space can then be computed analytically, see e.g. Werner (1994); Werner and Scheeres (1997); Scheeres et al. (1996). Each of these approaches has its own advantages and limitations, which are well documented in the literature. Comparative analyses of these methods have been the focus of numerous studies and can be found in various publications, e.g. Balmino (1994); Werner and Scheeres (1997); Hu (2012).

Unlike the previously mentioned approaches, in this paper we present a solution to the coupled interior-exterior BVP based on a numerical method. For this purpose, we define a spherical 3D computational domain centered at the gravity center of the selected celestial body, with a radius ten times larger than its average radius (similarly based ideas have been applied in Fašková et al. (2010); Yin and Sneeuw (2021); Duan et al. (2024)). Within this domain, we solve the Poisson equation for the gravitational potential, using the celestial

body's density distribution as input. Outside it, where the density of surrounding space is assumed to be zero, the Poisson equation reduces to the Laplace equation, see e.g. Moritz (1980). A Dirichlet BC is applied on the outer boundary of the domain, using the expression for the gravitational potential generated by a homogeneous sphere, see for example (Moritz 1980). It is worth noting that in our approach, we assume neither the presence of an additional body generating a gravitational field, nor the motion of the studied celestial object. The problem is then solved numerically by the finite element method (FEM). The result is the distribution of the gravitational potential and gravitational acceleration throughout the entire domain, that is, inside, on the surface, and outside the celestial body.

The paper is organized as follows. The first section formulates the coupled interior-exterior BVP for the gravitational potential. The second section presents its solution using FEM. The third section describes the numerical experiments, starting with a test case for evaluating the experimental order of convergence, followed by simulations involving irregular celestial bodies. Finally, the last section provides a summary and conclusions.

2 Formulation of the coupled interior–exterior boundary value problem

Let us consider an infinite domain containing a selected celestial object Ω_{CB} (see Fig. 1 a). To define the computational domain Ω for our purposes (specifically, to enable the subsequent application of FEM) we truncate this infinite space by introducing an artificial spherical boundary placed sufficiently far from the object (see Fig. 1 b) and with its origin located at the center of mass of the chosen celestial body.

Within this domain Ω, we formulate the following BVP

$$\Delta V(\mathrm{x}) = f(\mathrm{x}), \qquad \mathrm{x} \in \Omega, \tag{1}$$

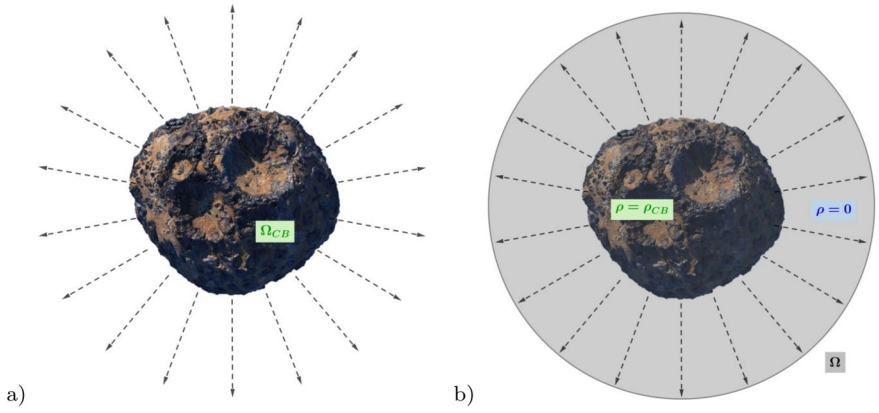

Fig. 1 An illustration of **a** the infinite domain containing a selected celestial body Ω_{CB} (e.g. the Psyche asteroid [24] in this case) and its surroundings, and **b** its truncation to the computational domain Ω for numerical purposes. Here, ρ_{CB} denotes the density of the celestial body, while outside it, a zero density $\rho = 0$ is assumed

$$V(\mathrm{x}) = \frac{GM}{R}, \qquad \mathrm{x} \in \partial\Omega, \tag{2}$$

where $V(\mathrm{x})$ is the gravitational potential at any point $\mathrm{x} = (x, y, z)$, G is the universal gravitational constant, M is the weight of a celestial object, and R is the radius of a spherical boundary $\partial\Omega$. We note that, as defined, BC (2) represents the gravitational potential generated by a homogeneous sphere when the point at which the potential is evaluated is located outside the body, see e.g. Moritz (1980).

The right-hand side of (1) is given by $f(\mathrm{x}) = -4\pi G\rho(\mathrm{x})$, where $\rho(\mathrm{x})$ is the density of the celestial body, when $\mathrm{x} \in \Omega_{CB}$. If $\mathrm{x} \in \Omega - \Omega_{CB}$, then $\rho(\mathrm{x}) = 0$. So from a mathematical point of view, BVP given by (1)-(2) consists of an elliptic partial differential equation with a discontinuous right-hand side and a Dirichlet BC. On the other hand from the perspective of physical geodesy, it represents a combination of the Poisson and Laplace equations, see e.g. Moritz (1980), with an approximate boundary condition of Dirichlet type, specified at a sufficient distance. Therefore, we will refer to BVP given by (1)-(2) as the coupled interior-exterior BVP.

3 Solution by the the finite element method

From the standard theory of partial differential equations, see e.g. Rektorys (1977), it follows that there exists a unique weak solution to the BVP (1)-(2). Furthermore, applying the general theory of FEM, see e.g. Brenner and Scott (2002), we know that the FEM solution converges to the weak solution.

To solve the BVP (1)-(2) by FEM, we adopt the fundamental principles outlined in Brenner and Scott (2002) and follow the approach presented in Reddy (2006).

We discretize the entire computational domain Ω into a union of elements Ω^e, $e = 1, \ldots, \mathcal{N}$, where $\mathcal{N}$ denotes the total number of elements in Ω. Since our computations involve the irregular shape of the celestial body, which we approximate using a set of triangles, we employ the linear tetrahedral elements defined by four nodes, N_j, $j = 1, ..., 4$, see Fig. 2 a.

To ensure that the resulting stiffness matrix is positive definite, we begin by multiplying equation (1) by -1, i.e., we rewrite equation (1) in the form (for the sake of clarity, we omit x in the subsequent equations)

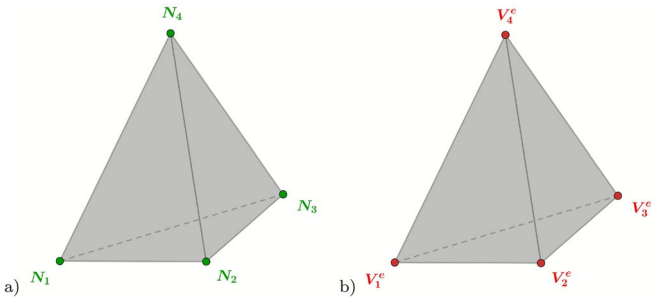

Fig. 2 An illustration of the notation: **a** the linear tetrahedral element Ω^e defined by four nodes N_j, $j = 1, \ldots, 4$, depicted in green, and **b** its unknown nodal values V_j^e, $j = 1, \ldots, 4$, depicted in red

$$-\Delta V = 4\pi G\rho. \tag{3}$$

Then we multiply (3) by a weight function w and using Green's identity we obtain the weak formulation of (1) over an arbitrary above defined element Ω^e

$$\int\limits_{\Omega^e} \nabla V \cdot \nabla w \,\mathrm{dx} = \int\limits_{\partial\Omega^e} \nabla V \cdot \mathrm{n}\, w \,\mathrm{d}\sigma + \int\limits_{\Omega^e} 4\pi G\rho\, w \,\mathrm{dx}, \tag{4}$$

where n denotes the unit outer normal to $\partial\Omega^e$.

For a linear tetrahedral element Ω^e with four nodes, see Brenner and Scott (2002) or Reddy (2006), we can write

$$V \approx V^e = \sum_{j=1}^{4} V_j^e \psi_j, \tag{5}$$

i.e. we take an approximation of the unknown value V as V^e, a linear combination of basis functions ψ_j with coefficients V_j^e, $j = 1, ..., 4$, see Fig. 2 b. It is worth noting that the linear basis functions on a tetrahedral element are defined such that each function is equal to 1 at one vertex of the tetrahedron and 0 at the other three, resulting in a linear variation of the solution within the element, see e.g. Brenner and Scott (2002); Reddy (2006).

Then we substitute (5) into the weak formulation (4), and consider ψ_i for weight function w. We obtain the i^{th} equation in the form

$$\begin{aligned} &\sum_{j=1}^{4} V_j^e \int\limits_{\Omega^e} \frac{\partial\psi_j}{\partial x}\frac{\partial\psi_i}{\partial x} + \frac{\partial\psi_j}{\partial y}\frac{\partial\psi_i}{\partial y} + \frac{\partial\psi_j}{\partial z}\frac{\partial\psi_i}{\partial z}\,\mathrm{dx} = \\ &= \int\limits_{\partial\Omega^e} q_n\, \psi_i \,\mathrm{d}\sigma + \int\limits_{\Omega^e} 4\pi G\rho\, \psi_i \,\mathrm{dx} \end{aligned} \tag{6}$$

where $q_n = \nabla V(\mathrm{x}) \cdot \mathrm{n}$ denotes the projection of the vector $\nabla V(\mathrm{x})$ along the unit outer normal n.

Now we can write (6) in a compact matrix form

$$\mathrm{K}^e\, \mathbf{V^e} = \mathrm{Q}^e + \mathrm{f}^e, \tag{7}$$

where $\mathrm{K}^e = [K_{ij}^e]$ denotes an element stiffness matrix, $\mathbf{V^e} = (V_1^e, ..., V_4^e)$ is a column vector of unknowns, Q^e and f^e denote the right-hand side vectors, namely the flux vector, derived from the gradient of the gravitational potential, and the source vector, which incorporates the density distribution, respectively.

Then the equations for all elements are assembled using two fundamental principles:

(i) Continuity of primary variables at interelement nodes. This means that the nodal values V_j^e and V_j^{e+1} of two adjacent elements Ω^e and Ω^{e+1} must be equal at their shared nodes.

(ii) Equilibrium (or balance) of secondary variables at element interfaces. This implies that, on portions of $\partial\Omega^e$ lying in the interior of the domain Ω, the value q_n^e on the side p of the element Ω^e cancels with the value q_n^{e+1} on the side r of the element Ω^{e+1}, provided that sides p and r coincide geometrically.

Finally, we impose the Dirichlet BC (2) at the nodes located on $\partial\Omega$. In this way, we obtain the global linear system of equations with the column vector of unknown global nodal values V

$$\mathrm{K\,V} = \mathrm{Q} + \mathrm{f}, \tag{8}$$

where K is a sparse and positive definite matrix, as most of its entries are zero, and Q and are column vectors whose components are also mostly zero, because the fluxes cancel inside the computational domain, and the source vector contains zero values in the region governed by the Laplace equation.

For readers interested in the details of FEM, we recommend, for instance, Reddy (2006).

4 Numerical experiments

All numerical simulations were performed in the FEM software package Ansys 2025 R1 [2]. Given that the Poisson and Laplace equations are mathematical simplifications of the general heat conduction equation, the problem was formulated and solved in ANSYS using a steady-state thermal analysis with the 'thermal conductivity' equal 1. The right-hand side of (1) was defined as a 'heat generation rate', with two separate domains characterized by different material densities, see Fig. 6. Consequently, in the solution visualizations, the gravitational potential was represented by the variable 'temperature', and the gravitational acceleration vector was analogously represented by the 'total heat flux'.

4.1 Validation of the proposed method via test case

As an initial validation step, we conducted a test case in which the gravitational field was generated by a homogeneous sphere of radius $1\,[m]$ and density $\rho_{HS} = 1\,[kg/m^3]$, while the whole computational domain Ω has the radius $2\,[m]$, see Fig. 3. The subscript *HS* in ρ_{HS} is intended to emphasize the assumption of a homogeneous sphere as the gravitating body.

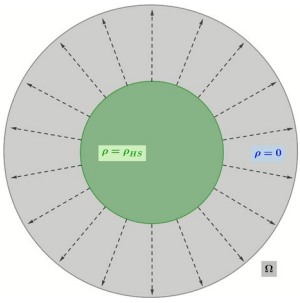

Fig. 3 The computational domain for the test experiment: a sphere with radius $1\,[m]$ and density $\rho_{HS} = 1$ (depicted in green), which generates the gravitational field, and a total domain Ω with radius $2\,[m]$ (depicted in green and grey)

Table 1 Testing numerical experiment – statistics of residuals in $\Omega - \Omega_{HS}$.

Mesh	Edge	Nodes	Avg	Min	Max	σ	EOC
1	0.5	3580	4.53e−06	1.14e−19	1.29e−04	2.128e−03	-
2	0.25	23653	6.01e−08	1.08e−21	5.10e−06	2.452e−04	2.161
3	0.125	179406	9.09e−10	3.74e−23	1.39e−07	3.015e−05	2.096
4	0.0625	1394955	1.35e−11	2.81e−25	7.62e−09	3.670e−06	2.106

The *Mesh* column denotes the level of mesh, the *Edge* column represents the edge length of the elements in [*m*], the *Nodes* column indicates the number of nodes in $\Omega - \Omega_{HS}$, the values *Avg*, *Min*, and *Max* indicate the average, minimum, and maximum values of the residuals, respectively, the σ column shows the standard deviation of the residuals, calculated as $\sigma = \sqrt{\frac{1}{Nodes}\sum_{i=1}^{Nodes}(residuals)^2}$ and the *EOC* stands for the experimental order of convergence

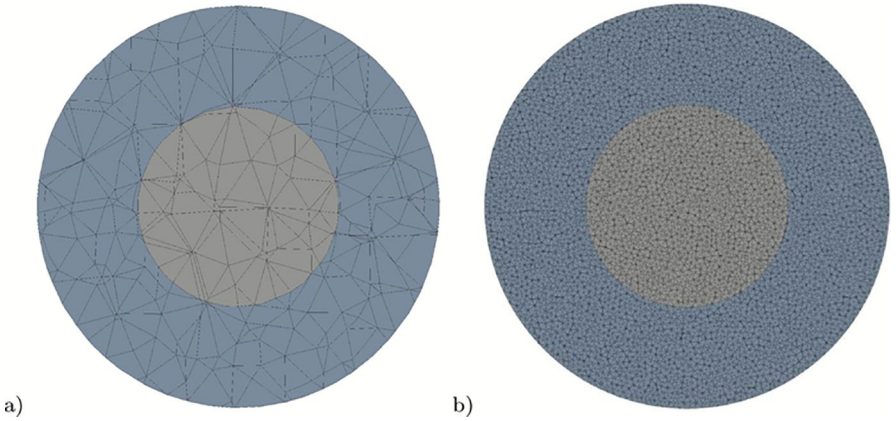

Fig. 4 The test experiment - cross-section of the computational domain discretized into elements: **a** the coarsest grid, **b** the finest grid

The computational domain has been meshed by tetrahedral elements with the length of edge $0.5\,[m]$, see Tab. 1 and Fig.4 a. Then a sequence of three uniform mesh refinements, see Fig.4 b, was performed in order to compute the experimental order of convergence (EOC) of the method. In general, the value of EOC might be calculated in the following way. Let us assume that E_h denotes the error corresponding to a mesh size *h*, the EOC between two successive meshes h_1 and h_2 is then calculated as

$$\mathrm{EOC} = \frac{\log\left(\frac{E_{h_1}}{E_{h_2}}\right)}{\log\left(\frac{h_1}{h_2}\right)}. \tag{9}$$

This value provides an estimate of the asymptotic convergence behavior of the numerical method. More details on the value of the EOC, along with a detailed derivation, can be found, for example, in Minarechová et al. (2021).

In our case, the obtained numerical solution, see Fig. 5, was evaluated against the analytical reference for homogeneous sphere $V = GM/R$. Results of this comparison for nodes located outside the gravitationg sphere, Ω_{HS}, can be found in Table 1. The proposed method exhibits second-order accuracy, as indicated by the EOC values as well as it clearly shows a decrease in the observed characteristics with mesh refinement.

4.2 Numerical simulations involving real celestial bodies

Building on the test case, we carried out three numerical experiments involving comet 67P/Churyumov–Gerasimenko, asteroids 25143 Itokawa and 433 Eros. For each case, we used a 3D triangularized model of the celestial body, obtained from the 3D Asteroid Catalogue [1]. In this setup, the given triangles naturally form the element faces, while their vertices serve as the mesh nodes. The meshing process then extends both inside and outside the celestial body.

4.2.1 Comet 67P/Churyumov–Gerasimenko

Comet 67P/Churyumov-Gerasimenko is a Jupiter-family comet. It became well-known because of the European Space Agency's Rosetta mission (Taylor et al. 2017) that was the first spacecraft to orbit a comet and to send a lander, called Philae, to its surface. The designation of the comet originates from the names of Klim Churyumov and Svetlana Gerasimenko, who discovered it in 1969. It has an unusual two-lobed shape, see Fig. 6 or Fig. 7, with an irregular geometry that is suitable for evaluating the performance of the method.

For our numerical simulation, a 3D computational domain Ω that contained a comet at its center, see Fig. 6, was created; while in Fig. 7 a) only the comet, discretized into tetrahedral elements, is visualized. The input physical parameter for the simulation was a uniform density 533 kg/m^3, see e.g. Yin and Sneeuw (2021). The Dirichlet BC was assigned a value of $2.2234 \times 10^{-2}\,[m^2 s^{-2}]$. A detail of a domain cross-section with equipotential contours displayed inside the comet and on its surface can be seen in Fig. 8. Fig. 9 shows the total gravitational acceleration vector. It is important to note that, in ANSYS, this quantity cor-

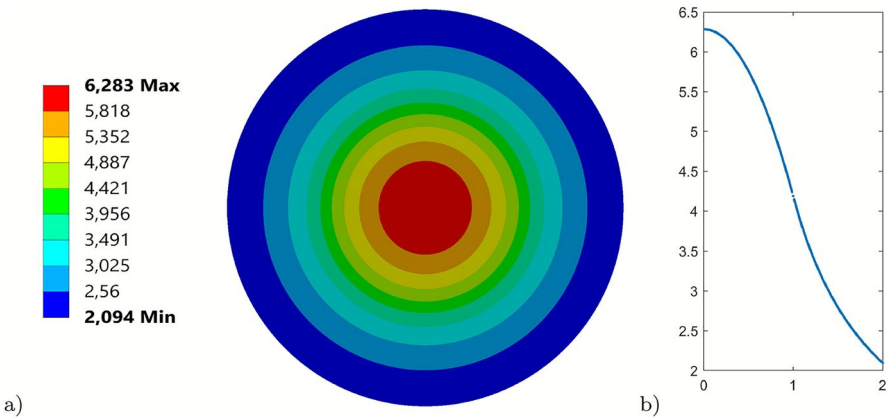

Fig. 5 The test experiment - gravitational potential solution: **a** cross-section of the computational domain Ω, **b** the nodal solution as a function of radius

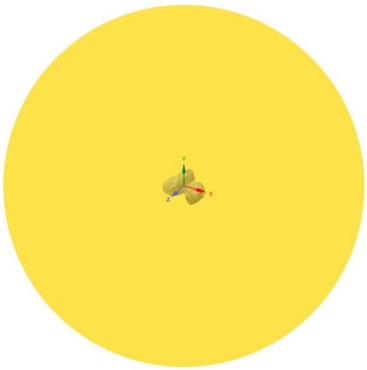

Fig. 6 The computational domain Ω for the experiment with comet 67P/Churyumov-Gerasimenko

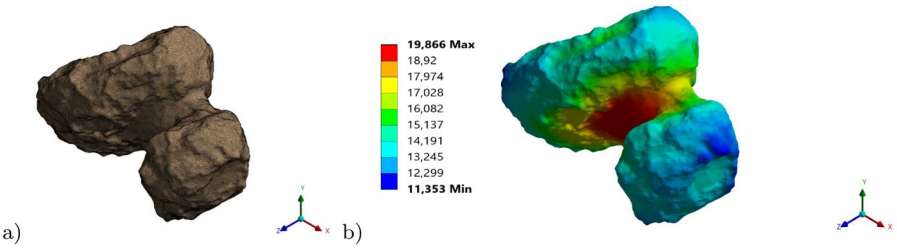

Fig. 7 The comet 67P/Churyumov-Gerasimenko: **a** meshed by tetrahedral elements, **b** gravitational potential distribution $[m^2 s^{-2}]$ on the its surface

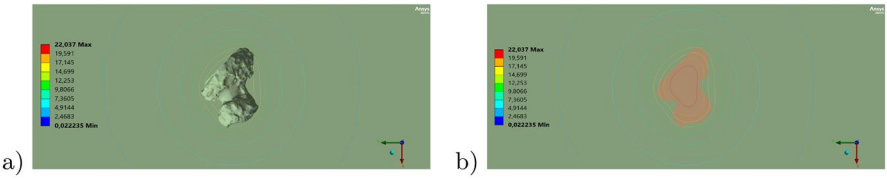

Fig. 8 Cross-section of the computational domain: equipotential contours of the gravitational potential $[m^2 s^{-2}]$ throughout the entire computational region including **a** within the comet, and **b** on the comet's surface

responds to the total heat flux, which results in the vectors pointing in opposite directions. The gravitational potential distribution on the comet's surface in views along the coordinate axes can be seen in Fig. 10. The obtained visualizations clearly demonstrate agreement with the solutions obtained using other methods, see e.g. Yin and Sneeuw (2021).

4.2.2 Asteroid (25143) Itokawa

As the second object of interest in our analysis, we selected an asteroid (25143) Itokawa. It is an S-type near-Earth asteroid approximately 330 m in length and an irregular shape. The Japanese Hayabusa spacecraft conducted a rendezvous, landing, and sample-return mission

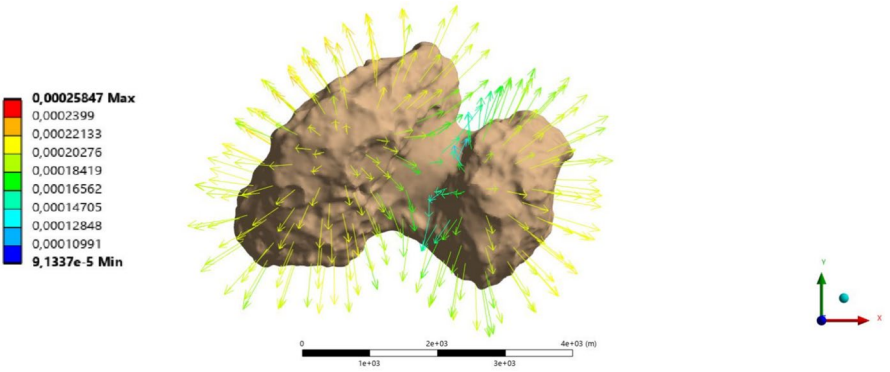

Fig. 9 Comet 67P/Churyumov-Gerasimenko - total gravitational acceleration vector $[ms^{-2}]$ on the surface of the asteroid

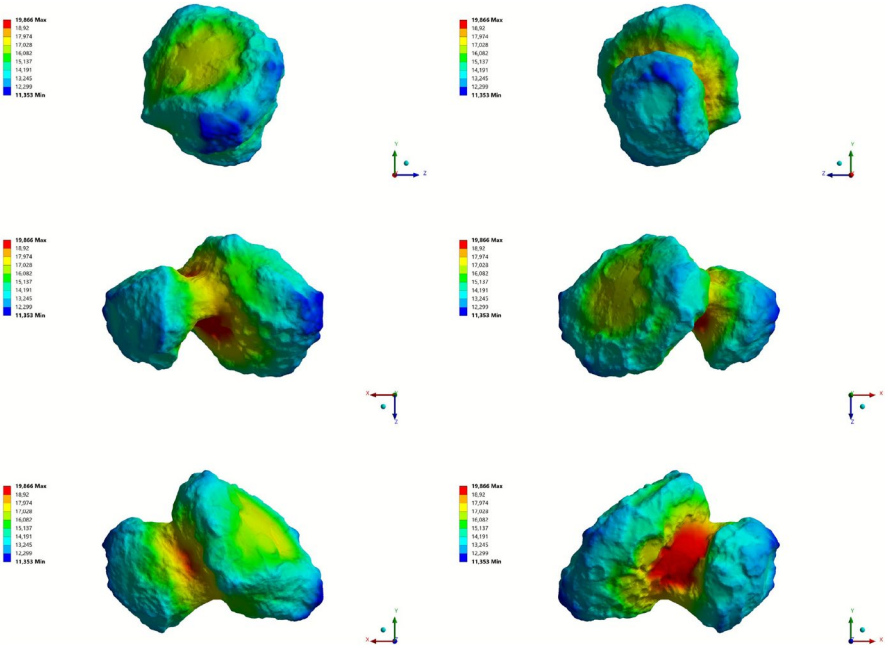

Fig. 10 The gravitational potential distribution $[m^2s^{-2}]$ on the comet 67P/Churyumov-Gerasimenko's surface in views along the coordinate axes

in 2005, confirming that Itokawa is a rubble-pile structure composed of loosely bound boulders and regolith (Tsuda et al. 2013; Yoshikawa et al. 2021).

For our numerical simulation, we again created a 3D computational domain Ω with a radius ten times larger than the average dimension of the asteroid, and with the asteroid located at its center of mass. The input data for our simulation included a 3D model [1], a uniform density 1 950 kg/m^3, and the value of the Dirichlet BC $4,6145 \times 10^{-4}$ $[m^2s^{-2}]$. The total number of the finite elements in the whole computational domain Ω has been 4

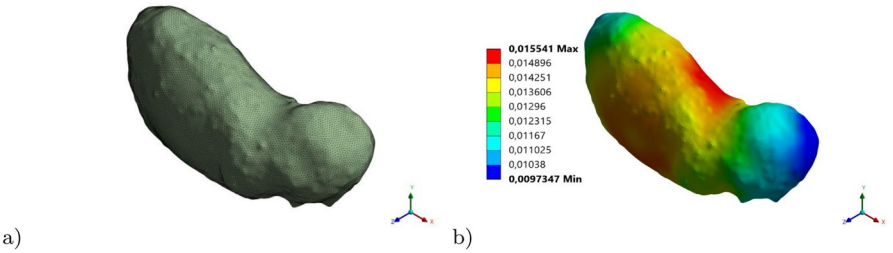

Fig. 11 **a** The surface of asteroid Itokawa approximated by a set of triangles, **b** gravitational potential distribution $[m^2 s^{-2}]$ on the its surface

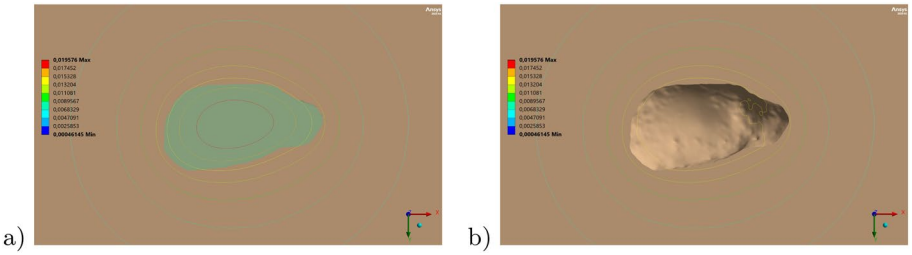

Fig. 12 Asteroid (25143) Itokawa - Cross-section of the computational domain: equipotential contours of the gravitational potential $[m^2 s^{-2}]$ throughout the entire computational region, including **a** within the body, and **b** on the body's surface

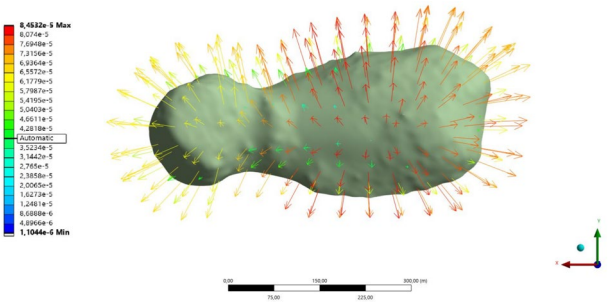

Fig. 13 Asteroid (25143) Itokawa - total gravitational acceleration vector $[ms^{-2}]$ on the surface of the asteroid. We remind that since in ANSYS the vectors represent heat flux, they have an opposite orientation to that of the gravitational vectors

984 273, while the total number of nodes on the asteroid's surface 73 498. The discretized 3D model of asteroid Itokawa is depicted in Fig. 11 a.

The corresponding solution for the gravitational potential on its surface is depicted in Fig. 11 b, while shown in views along the coordinate axes, is presented in Fig. 14. As in the previous experiment, a domain cross-section was generated too, with isolines used to visualize the spatial distribution of the gravitational potential (see Fig. 12). As a final step, we included a visualization of the gravitational acceleration vectors, see Fig. 13.

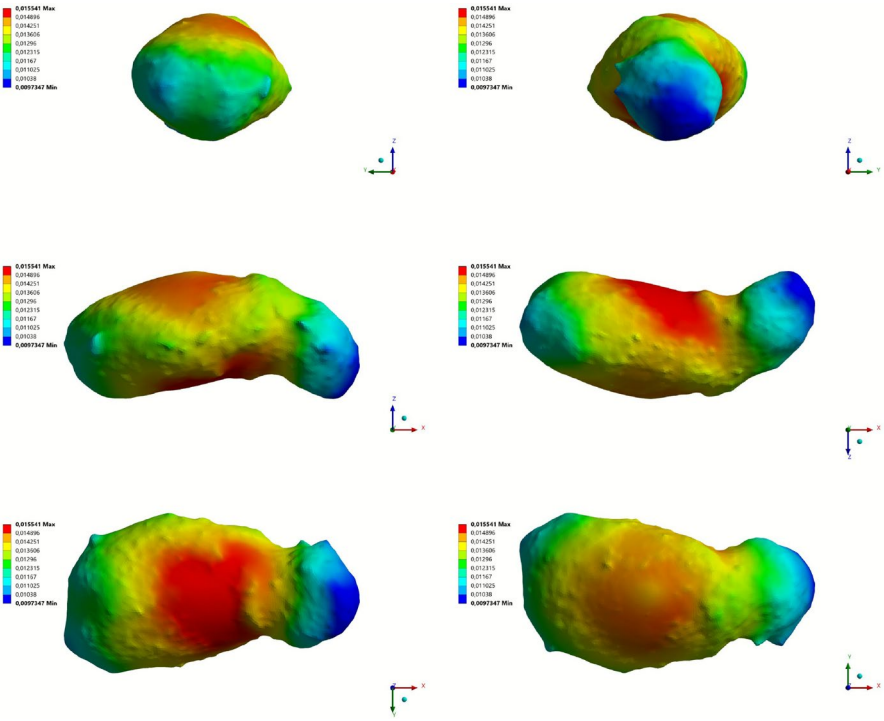

Fig. 14 Asteroid (25143) Itokawa - gravitational potential distribution $[m^2 s^{-2}]$ on the asteroid's surface in views along the coordinate axes

4.2.3 Asteroid (433) Eros

The final celestial object chosen for our analysis was asteroid (433) Eros. It is a large near-Earth asteroid about 34 kms long with an irregular shape and many craters. We selected this asteroid due to its significantly larger size compared to the previously studied asteroid, Itokawa.

For the purpose of our numerical simulation, a three-dimensional computational domain Ω was created once more, having a radius ten times greater than the asteroid's average dimension, with the asteroid positioned at its center of mass. The input physical parameter for this experiment included a density of 2 670 kg/m^3 and the Dirichlet BC $4.46615 \times 10^{-7}\,[km^2 s^{-2}]$. Afterwards, the computational domain was meshed by 441 778 finite elements, and the number of nodes on the asteroid's surface was 148 164. The 3D model of asteroid Eros [1], discretized with tetrahedral elements is depicted in the Fig. 15 a.

The gravitational potential solution, see Fig. 15 b, visualized from perspectives along the coordinate axes, is presented in Fig. 17. In line with the previous experiments, a cross-sectional view of the domain was also created, with the gravitational potential depicted by isolines to demonstrate its spatial distribution (see Fig. 16). Finally, we visualized the gravitational acceleration vectors, as shown in Fig. 18. Again we remind that as the vectors in ANSYS represent heat flux, their orientation is opposite to that of the gravitational vectors.

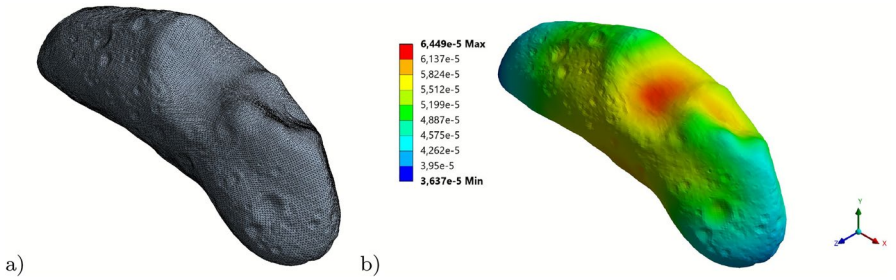

Fig. 15 **a** The 3D model of asteroid (433) Eros meshed with tetrahedral elements, **b** the gravitational potential distribution $[km^2s^{-2}]$ on its surface

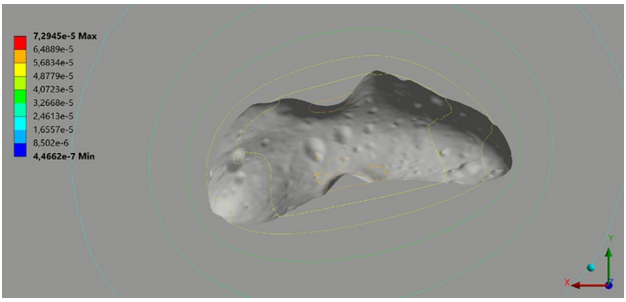

Fig. 16 Asteroid (433) Eros - Cross-section of the computational domain: equipotential contours of the gravitational potential $[km^2s^{-2}]$ throughout the computational domain including the body's surface

5 Discussion and conclusions

In this work, we have proposed, derived, and implemented a finite element method-based approach for modeling the gravitational field of irregular celestial bodies. To this end, we formulated a coupled interior-exterior boundary value problem, consisting of a partial differential equation with a discontinuous right-hand side and a Dirichlet boundary condition. Solving such a formulated problem allowed us to obtain the distribution of the gravitational potential not only on the surface of the body but also within its interior and surrounding space. We validated the proposed approach using a test case involving a homogeneous sphere, where the convergence was shown to be of second order. Subsequently, we applied it to three real celestial objects of significantly different sizes and irregular shapes, namely, comet 67P/Churyumov-Gerasimenko, and the asteroids 25143 Itokawa and 433 Eros, to demonstrate its effectiveness. The outcome was the spatial distribution of the gravitational potential and gravitational acceleration. The results confirm that the proposed method is robust enough to handle geometries of considerable complexity.

In the future, we plan to compare the proposed approach with other methods in terms of both accuracy and computational efficiency. Furthermore, based on the current problem formulation and proposed methodology, future extensions could include incorporating a variable density model or accounting for multiple interacting bodies. Another promising direction would be the dynamic modeling of evolving celestial bodies.

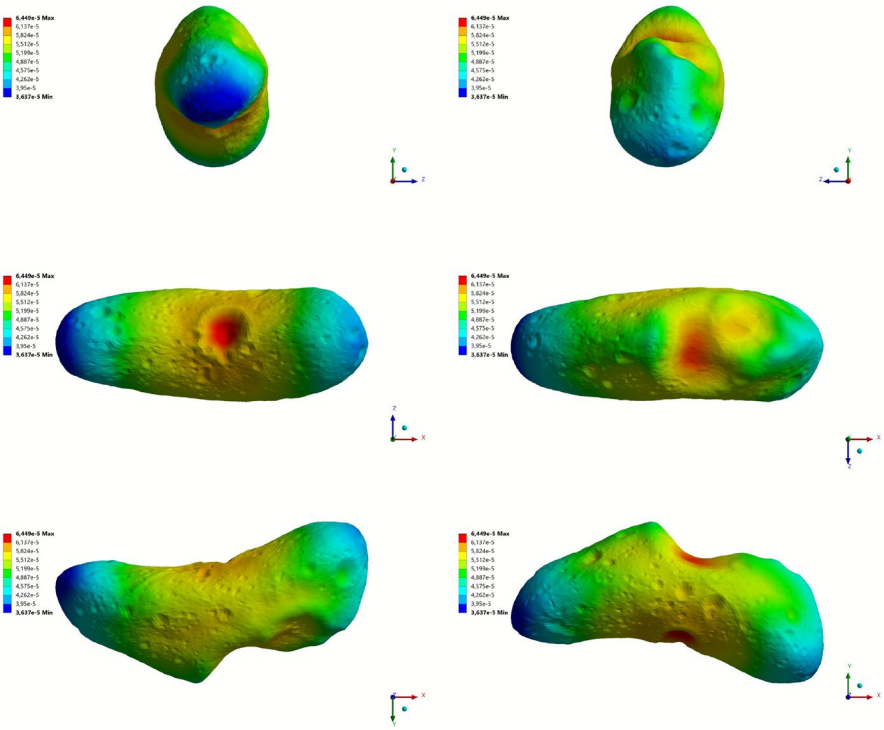

Fig. 17 Asteroid (433) Eros - Gravitational potential distribution $[km^2 s^{-2}]$ on the asteroid's surface

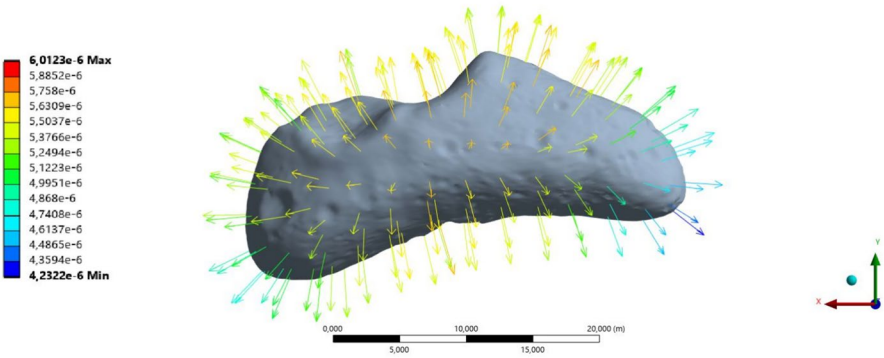

Fig. 18 Asteroid (433) Eros - total gravitational acceleration vector $[km\, s^{-2}]$ on the surface of the asteroid

Acknowledgements This work was supported by Grants VEGA 1/0249/24 and 1/0690/24, APVV-23-0186, and KEGA 010STU-4/2025

Author Contributions MM proposed the initial ideas and performed the numerical experiments. ZM contributed to develop the theory and wrote the manuscript. KM contributed to develop the theory and devised the project. All authors discussed the results and contributed to the final version of the manuscript.

Data Availability All datasets generated and/or analysed within the experiments are available from the corresponding author.

Declarations

Conflict of interest All authors declare that they have no Conflict of interest.

References

3D Asteroid Catalogue: https://3d-asteroids.space/ (Accessed: July 8, 2025)
Ansys - Engineering Simulation Software: https://www.ansys.com/ (Accessed: July 8, 2025)
Asteroid Psyche: https://science.nasa.gov/solar-system/asteroids/16-psyche/ (Accessed: July 8, 2025)
Balmino G (1994) Gravitational potential harmonics from the shape of an homogeneous body. Celestial Mech Dyn Astr 60:331–364. https://doi.org/10.1007/BF00691901
Brenner SC, Scott LR (2002) The mathematical theory of finite element methods. Springer-Verlag, New York
Bucha B, Sansó F (2021) Gravitational field modelling near irregularly shaped bodies using spherical harmonics: a case study for the asteroid (101955) Bennu. J Geod 95:56. https://doi.org/10.1007/s00190-021-01493-w
Bucha B, Hirt C, Kuhn M (2019) Divergence-free spherical harmonic gravity field modelling based on the Runge-Krarup theorem: a case study for the Moon. J Geod 93:489–513. https://doi.org/10.1007/s00190-018-1177-4
Chanut TGG, Aljbaae S, Carruba V (2015) Mascon gravitation model using a shaped polyhedral source. Mon Not Roy Astron Soc 450(4):3742–3749
Colagross A, Ferrari F, Lavagna M et al (2015) Dynamical evolution about asteroids with high fidelity gravity field and perturbations modeling AAS/AIAA Astrodynamics Specialist Conference. Vail, Colorado, USA
Duan Y, Yin Z, Zhang K, Zhang S, Wu S, Li H, Zheng N, Bian Ch (2024) Modeling the gravitational field of the ore-bearing asteroid by using the CFD-based method. Acta Astronaut 215:664–673
Fašková Z, Čunderlík R, Mikula K (2010) Finite element method for solving geodetic boundary value problems. J Geodesy 84(2):135–144
Gao A, Liao W (2019) Efficient gravity field modeling method for small bodies based on Gaussian process regression. Acta Astronaut 157:73–91
Geissler P, Petit JM, Durda D, Greenberg R, Bottke W, Nolan M, Moore J (1996) Erosion and ejecta reaccretion on 243 ida and its moon. Icarus 120:140–157
Hu X (2012) A comparison of ellipsoidal and spherical harmonics for gravitational field modeling of non-spherical bodies, OSU Geodesy Report no. 499
Laplace PS (1785) Théorie de l'attraction des sphéroïdes et de la figure des planètes, Mémoires de l'Académie Royale des Sciences, Paris
Laplace PS (1799) Traité de Mécanique Céleste, Vol. 1, Paris: Duprat
Legendre AM (1782) Recherches sur la figure des planètes, Mémoires de l'Académie Royale des Sciences
Macák M, Minarechová Z, Tomek L, Čunderlík R, Mikula K (2023) Solving the fixed gravimetric boundary value problem by the finite element method using mapped infinite elements. Computational Geosciences 27(4):649–662
March RE (2021) OSIRIS-REx: a NASA Asteroid Space Mission. Int J Mass Spectrom 469:116677
Minarechová Z, Macák M, Čunderlík R, Mikula K (2021) On the finite element method for solving the oblique derivative boundary value problems and its application in local gravity field modelling. J Geodesy 95:70
Moritz H (1980) Advanced Physical Geodesy. Herbert Wichmann Verlag, Karlsruhe
Olkin CB et al (2021) Lucy mission to the trojan asteroids: instrumentation and encounter concept of operations planet. Planet Sci J 2:172
Park RS, Werner RA, Bhaskaran S (2010) Estimating small-body gravity field from shape model and navigation data. J Guid Contr Dynam 33(1):212–221
Reddy JN (2006) An Introduction to the Finite Element Method, 3rd edn. McGraw-Hill Education, New York (**ISBN: 9780072466850**)
Rektorys K (1977) Variational Methods in Mathematics, Science and Engineering, Springer. Dordrecht. https://doi.org/10.1007/978-94-011-6450-4
Sanso F, Sideris MG (eds) (2013) Geoid determination: theory and methods. Springer, Berlin

Scheeres DJ, Werner RA, Bottke WF (1996) Polyhedral gravity model for asteroids. J Guid Control Dyn 19(5):1143–1150
Sebera J, Bezdek A, Pešek I, Henych T (2016) Spheroidal models of the exterior gravitational field of asteroids Bennu and Castalia. Carus 272:70–79
Šprlák M, Han SC, Featherstone WE (2020) Spheroidal forward modelling of the gravitational fields of 1 Ceres and the Moon. Icarus 335:113412
Takahashi Y, Scheeres D (2013) Surface gravity fields for asteroids and comets. AIAA J Guid Control Dyn 36:362–374
Taylor MGGT, Altobelli N, Buratti BJ, Choukroun M (2017) The Rosetta mission orbiter science overview: the comet phasePhil. R. Soc, Trans. A. 375(2097):20160262. https://doi.org/10.1098/rsta.2016.0262
Tsuda Y, Yoshikawa M, Abe M, Minamino H, Nakazawa S (2013) System design of the Hayabusa 2–Asteroid sample return mission to 1999 JU3. Acta Astronaut 91:356–362
Werner R (1994) The gravitational potential of a homogeneous polyhedron or polyhedral shell. Celest Mech Dyn Astron 59(3):253–278
Werner R, Scheeres D (1997) Exterior gravitation of a polyhedron derived and compared with harmonic and mascon gravitation representations of asteroid 4769 Castalia. Celest Mech Dyn Astron 65:313–344
Yin Z, Sneeuw N (2021) Modeling the gravitational field by using CFD techniques. J Geod 95:68. https://doi.org/10.1007/s00190-021-01504-w
Yoshikawa M, Kawaguchi J, Fujiwara A, Tsuchiyama A (2021) Chapter 6 - The Hayabusa mission. Elsevier, Sample Return Missions, pp 123–146
Zuber MT, Park RS, Elkins-Tanton LT et al (2022) The Psyche Gravity Investigation. Space Sci Rev 218:57. https://doi.org/10.1007/s11214-022-00905-3